Title

Imaging interfacial electrical transport in graphene–MoS2 heterostructures with electron-beam-induced-currents

Journal

Applied Physics Letters, 107(22)

ISSN

0003-6951

Authors

White, ER
Kerelsky, Alexander
Hubbard, William A
et al.

Publication Date

2015-11-30

DOI

10.1063/1.4936763

Peer reviewed

Imaging interfacial electrical transport in graphene-MoS_2 heterostructures with electron-beam-induced-currents

E. R. White,[1,a)] Alexander Kerelsky,[1] William A. Hubbard,[1] Rohan Dhall,[2] Stephen B. Cronin,[2] Matthew Mecklenburg,[3] and B. C. Regan[1,b)]

[1]*Department of Physics & Astronomy and California NanoSystems Institute, University of California, Los Angeles, California, 90095, USA*

[2]*Department of Electrical Engineering, University of Southern California, Los Angeles, California, 90089, USA*

[3]*Center for Electron Microscopy and Microanalysis, University of Southern California, Los Angeles, California, 90089, USA*

Abstract: Heterostructure devices with specific and extraordinary properties can be fabricated by stacking two-dimensional crystals. Cleanliness at the inter-crystal interfaces within a heterostructure is crucial for maximizing device performance. However, because these interfaces are buried, characterizing their impact on device function is challenging. Here we show that electron-beam induced current (EBIC) mapping can be used to image interfacial contamination and to characterize the quality of buried heterostructure interfaces with nanometer-scale spatial resolution. We applied EBIC and photocurrent imaging to map photo-sensitive graphene-MoS_2 heterostructures. The EBIC maps, together with concurrently-acquired scanning transmission electron microscopy (STEM) images, reveal how a device's photocurrent collection efficiency is adversely affected by nanoscale debris invisible to optical-resolution photocurrent mapping.

Two-dimensional (2D) crystals can be stacked to form layered heterostructures with the potential to show a tremendous variety of extraordinary properties, ranging from itinerant magnetism to superconductivity[1]. The performance of a layered heterostructure depends crucially on the layer interfaces, the quality of which is determined by the constituent materials[2,3] and any impurities introduced during fabrication[4]. Layered heterostructures are usually fabricated using some combination of the traditional wet process[3,5,6], the "dry" method[2,7–11], or the "dry peel" method[3,12,13]. Though efforts to improve device cleanliness are ongoing, contaminants are invariably introduced into the critical inter-layer spaces by the currently available transfer techniques[4].

Most interface-characterization techniques can either locate impurities and adsorbates, or evaluate their effect on an interface's electronic properties. Global device transport measurements of, for example, resistance or charge mobility provide a crude, blind metric; they serve as an indirect gauge for interface quality but alone they give no specific information about the location and composition of impurities. In this category, capacitance spectroscopy has proved particularly

[a)] Electronic mail: ewhite@physics.ucla.edu
[b)] Electronic mail: regan@physics.ucla.edu

powerful[3]. Coupling such transport measurements with spatially-resolved characterization techniques has enabled convincing demonstrations of importance of interface cleanliness[3,4]. However, the standard mapping techniques – optical microscopy, scanning electron microscopy (SEM), atomic force microscopy (AFM), and cross sectional transmission electron microscopy (TEM)[3,4] – do not probe the interfacial electronic properties directly. Thus the causal relationship between contamination or transfer residue and poor transport characteristics must be inferred from their correlated appearance.

An ideal technique for characterizing the interface quality in layered heterostructures would combine local transport measurements with high-resolution, plan-view imaging of the geometry. Here we describe scanning TEM imaging of electron-beam induced currents[14–16] (STEM-EBIC) in a photovoltaic graphene/molybdenum disulfide/graphene (GMG) heterostructure. Unlike many layered heterostructure devices, the GMG heterostructure provides a photoresponse[9,17] that is a native, position-sensitive interface diagnostic. This diagnostic allows direct comparison of the STEM EBIC data with the transport properties most relevant to the device's intended function. Thus the GMG heterostructure is especially suited for an examination of interfacial quality.

Our heterostructures were fabricated by mechanical exfoliation of natural graphite (NGS Naturgraphit GmbH Graphenium Flakes) and single crystal MoS_2 (SPI Supplies 429MM-AB). Graphene and MoS_2 were deposited from Scotch tape onto a silicon substrate coated with 90 nm of SiO_2, the optimal thickness for optical identification of graphene[18]. Heterostructures were fabricated via three consecutive wet transfers. (After each wet transfer the sample was annealed for 30 minutes in air on a hot plate set to 300 °C.) To transfer a thin crystal, a PMMA backing layer was spun onto the substrate hosting the exfoliated crystal[6]. The oxide was then etched in 2 M NaOH leaving the thin crystal attached to the PMMA floating in solution. After multiple dips in de-ionized water the PMMA/thin crystal was positioned over its target using micromanipulators. Once a sample dried, its PMMA was partially dissolved using a few drops of fresh PMMA (4% in anisole). Acetone, isopropanol, and de-ionized water rinses removed the remaining residue. In this manner, monolayer or few-layer ($\lesssim$ 5 layers based on the optical contrast) graphene was first transferred onto thin MoS_2. Next the graphene-MoS_2 stack was transferred onto a second few-layer graphene sheet. The completed heterostructure was then transferred onto a silicon chip with pre-deposited platinum electrodes and a silicon nitride window. This transfer order ensures that PMMA is never spun onto any interface that will ultimately reside inside the heterostructure. Figure 1 shows a perspective schematic of the device. The optical and He ion images in Figure 2 show a typical completed device with the graphene layers sandwiching the ~50 nm-thick MoS_2 and contacting the platinum electrodes.

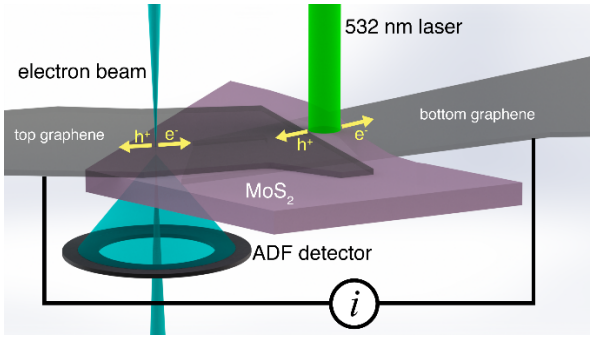

FIG 1: Schematic diagram of the heterostructure device and experimental setup for both EBIC and photocurrent measurements.

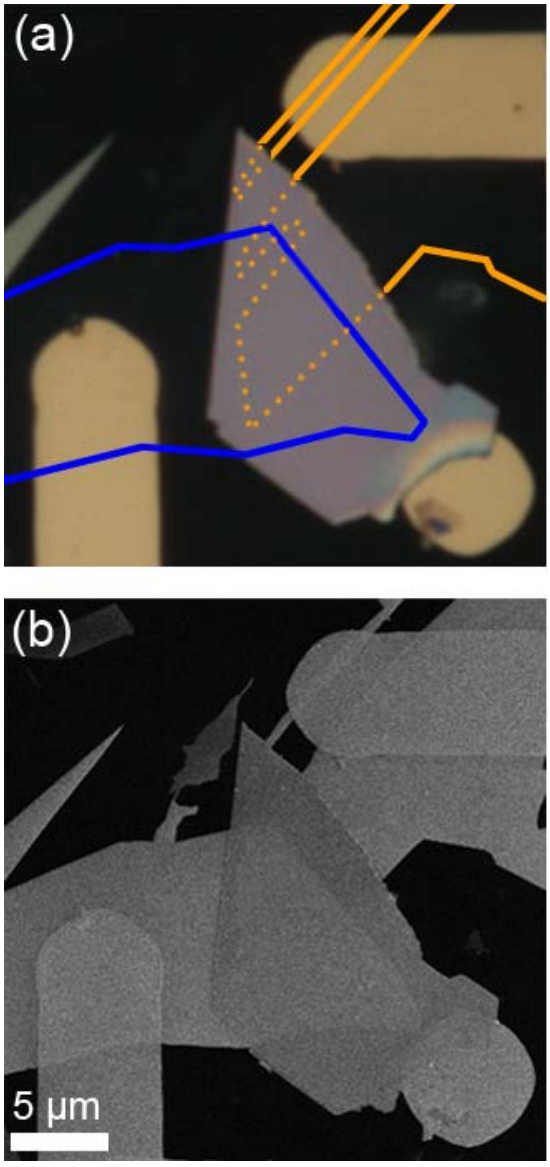

FIG 2: (a) Optical image of a GMG heterostructure wired to platinum electrodes on an electron-transparent Si_3N_4 membrane. The purple flake in the center of the image is MoS_2. The top and bottom-graphene layers are outlined in blue and orange respectively. The arms extending from the bottom and right sides are the platinum electrodes and the similarly colored circle is a platinum alignment marker. (b) He ion microscope image of the same device. Images (a) and (b) are displayed at the same magnification and share the same scale bar.

Photocurrent and STEM-EBIC measurements are conceptually very similar; in both cases a localized probe beam produces electron-hole pairs in the circuit as it is scanned across the sample. Photocurrent and EBIC maps are generated by measuring the current generated as the probe is rastered across the sample. Figure 1 illustrates the experimental set up (the two techniques are applied separately). The Schottky barrier at the graphene-MoS_2 interface produces an electric field inside the device that separates the charge carriers[9,17]. Photocurrents were measured with a Keithley 2400 Sourcemeter, and EBIC currents were measured with a FEMTO DLPCA-200 variable gain, low noise, transimpedance amplifier. A STEM beam dwell time of 2 ms ensured

that each pixel was an independent EBIC measurement, and that the resultant map's resolution was not limited by the amplifier bandwidth of 7 kHz. During STEM-EBIC measurements the EBIC and the annular dark field (ADF) detector signals were simultaneously digitized and associated with the contemporaneous position of the rastering electron beam to yield a pair of images. To prevent beam-induced deposition of hydrocarbons on the sample during EBIC imaging, the sample holder was cleaned and baked at ~100° C.

Photocurrent and STEM-EBIC maps on pristine heterostructures showed little contrast variation within architecturally uniform regions. However, exposing a heterostructure to a dose of ~100 $e^-/Å^2$ at 80 kV in the TEM revealed finer features in the EBIC map, presumably by introducing defects in the MoS_2 and decreasing the minority carrier diffusion length. Applying this dose produced a stable device; subsequent EBIC and photocurrent maps showed no further evolution of the transport properties. Prior to the dose treatment the Figure 2 device's maximum external quantum efficiency (EQE) was 13% [the EQE is defined as the ratio (photoelectron production rate/photon incidence rate)]. Afterwards, the EQE was 10%. Both values are comparable to those previously reported for similar graphene-MoS_2 heterostructures measured under comparable illumination conditions and no applied bias or gate[9,17]. All photocurrent and EBIC maps shown here were acquired after the dose treatment.

We obtained photocurrent maps by scanning a 3μW 532 nm laser focused to a ~1μm spot across the heterostructure and measuring the photogenerated current at each beam position. Figure 3(a) shows the photocurrent map for the device pictured in Figure 2. The large blue and orange features correspond to the overlap of the MoS_2 with the top and bottom-graphene layers, respectively. In regions where only one graphene layer is in contact with the MoS_2, current flows towards the MoS_2 relative to that particular interface. Where the MoS_2 has graphene on both sides the photocurrent signal is strongest and flows away from the bottom-graphene electrode, as seen previously on similar heterostructures[9,17].

The identifiable features in the photocurrent map are all present in the EBIC map of the same device (Figure 3b). Both Figure 3(a) and Figure 3(b) show the same gross spatial variation of the induced current in the MoS_2, which clearly is dominated by the overlap with the top and the bottom-graphene electrodes. The currents observed at common features are the same sign and qualitatively similar regardless of whether they are photo- or electron-induced. Subtle features, such as the dark, narrow strip bisecting the bottom-graphene/MoS_2 overlap at the top-graphene's right-hand edge are evident in both images, but are seen far more clearly in the EBIC image. Thus the photocurrent and EBIC measurements probe similar device physics.

One quantitative difference between the two maps is the magnitude of the negative photocurrent at the top-graphene/MoS_2 interface (blue region): it is relatively larger in the photocurrent image. This discrepany likely arises because the MoS_2 is transparent to 80 keV electrons but not optical photons. Thus the incident light produces more electron-hole pairs near the top-graphene/MoS_2 interface than near the bottom, generating a correspondingly larger signal from the top interface in the photocurrent measurement.

To quantify the resolution difference between the photocurrent and EBIC maps we estimate the resolution by measuring the distance between the 90% and 10% levels of the full contrast change[19] seen at the top-graphene step-edge (see Figure SI1)[20]. For photocurrent, this distance is 0.6 μm, implying resolution set by the diffraction-limited laser spot size. For STEM-EBIC, the intentsity drop at the edge occurs within one or two pixels, thus the resolution is limited by the 40 nm pixel size. Even at this relatively low magnification, the STEM EBIC resolution is ~10× better than that of the photocurrent map. At the sample boundary both techniques are likely

fundamentally limited by their corresponding probe sizes, which implies that STEM EBIC could show 1000× better spatial resolution (see Figure SI2 caption)[20].

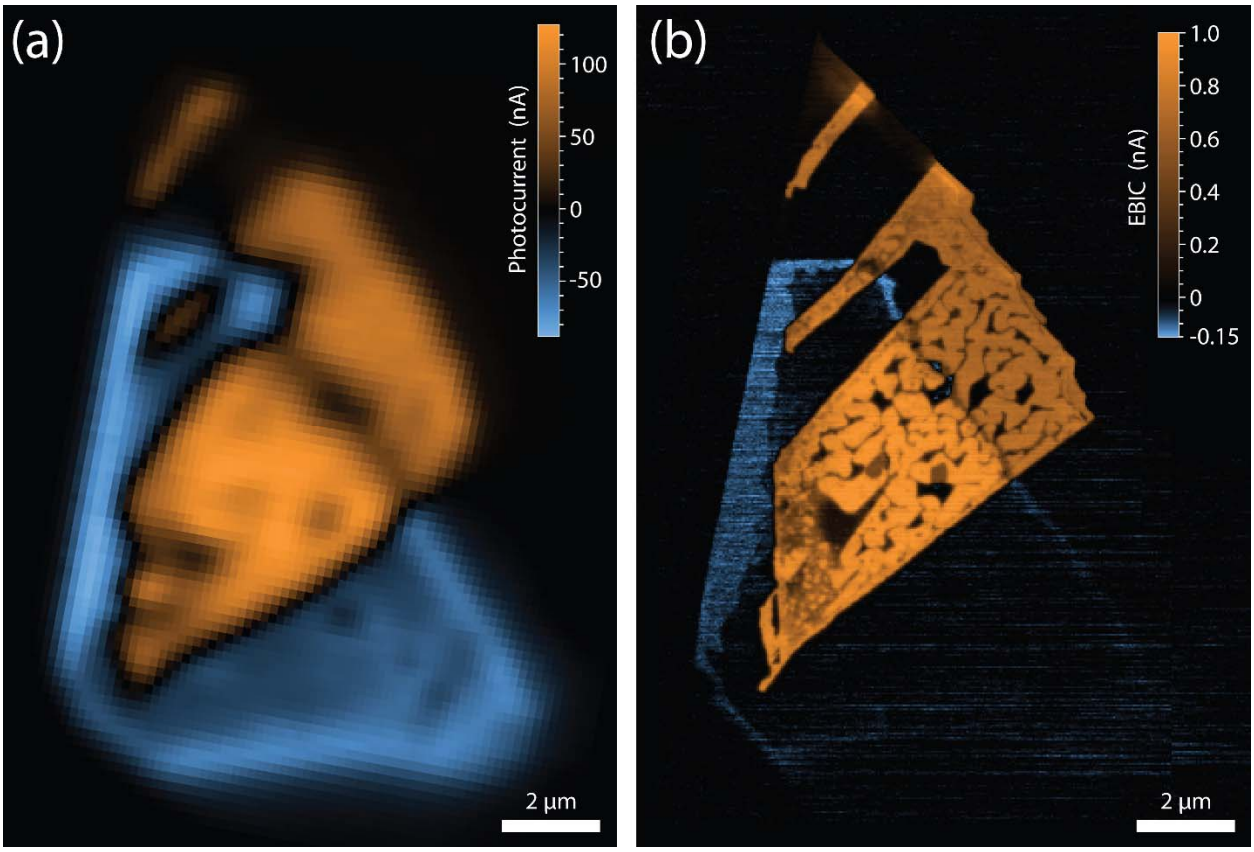

FIG 3: (a) Photocurrent and (b) EBIC maps of the device shown in Figure 2. Positive current flows away from the bottom-graphene electrode (orange) and negative current flows away from the top-graphene electrode (blue) in both maps.

Away from the lateral boundaries of the constituent materials, the photocurrent map (Figure 3a) shows mostly uniform contrast with some micron-sized dark spots. With its superior spatial resolution, the EBIC map (Figure 3b) reveals the morphology of these dark spots, as well as features not seen in the photocurrent map. A network of dark patches connected by thin dark lines is apparent, with the patch size ranging from ~100 nm to 2 µm. Darkness signifies near-zero induced current, and thus dark regions represent localized areas of poor current collection efficiency. The dark patches stretch smoothly across the edge of the top-graphene, indicating that the features are generated at the bottom-graphene/MoS_2 interface.

Because of their smooth, curved edges, we attribute these patches to residue from the wet transfer process. Similar structures have been seen and so-attributed in previous studies of interfacial cleanliness in heterostructure devices[3,4]. While contamination at such interfaces appears to be a universal problem, so also is this perhaps beneficial tendency for the contamination to aggregate in bubbles or pockets. With STEM-EBIC we see directly that the desired, efficient interfacial electronic transport observed in the clean regions is degraded within these pockets.

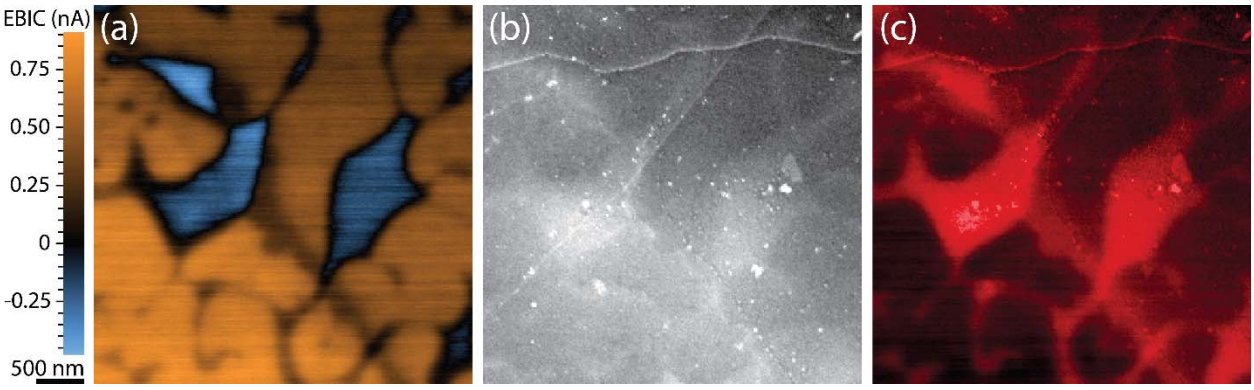

FIG 4: (a) Higher magnification EBIC map and (b) simultaneously acquired ADF image of the device shown in Figure 3. (c) Colorized composite image generated by multiplying the ADF image and the EBIC image with inverted contrast, producing high intensity regions corresponding to large ADF and low EBIC signals. These high intensity (more red) regions represent local regions of poor interfacial connection with the MoS_2 and bottom-graphene electrode.

To further characterize these regions of poor current collection efficiency we acquired higher magnification STEM-EBIC and ADF STEM images (Figure 4). The edge of the top-graphene layer extends from the top left to bottom right of the images, and is evident in the EBIC map as the dark strip separating the lower left and upper right regions of different average intensity. The dark patches in the EBIC image coincide with regions of enhanced ADF signal relative to the immediate surroundings. This correlation is seen more easily in Figure 4(c), which is generated by inverting (a) and multiplying it by (b), resulting in bright regions where the EBIC signal is low and the ADF signal is large. Contamination at the bottom-graphene/MoS_2 interface explains both signal changes. The additional mass in the contaminated regions scatters more electrons into the ADF detector. The contamination causes poor local connection at the interface, preventing efficient charge separation and decreasing the EBIC signal. The EBIC map shows, in plan-view, the effect of contamination on the local electrical properties of the GMG heterostructure.

Repeating the 90%-10% estimate described earlier, we find that the intensity step between a bright pocket and the dark strip in Figure 4(a) occurs in a distance of 70 nm (see Figure SI2)[20]. At this magnification the resolution is not limited by the pixel size, as it was in Figure 3(b). While passage through the 50 nm-thick MoS_2 increases the beam diameter to ~4 nm, this scale is still significantly smaller than the EBIC resolution. Thus the probe size is not limiting, as in photocurrent mapping. In fact, inside the device the STEM-EBIC resolution is determined by the minority carrier diffusion length[14], which has been decreased from its pristine value by the dose effects described earlier. This resolution outstrips that possible in SEM-EBIC, which is generally limited by the penetration depth in an electron-opaque sample[14]. As demonstrated here, STEM-EBIC has the high-resolution necessary to reveal otherwise invisible defects, and provides a direct measure of these defects' impact on a heterostructure device's electronic function.

This work has been supported by FAME, one of six centers of STARnet, a Semiconductor Research Corporation program sponsored by MARCO and DARPA, and by National Science Foundation Award DMR-1206849. The authors acknowledge the use of instruments at the Electron Imaging Center for NanoMachines supported by NIH 1S10RR23057 and the CNSI at UCLA, and the Zeiss center in Peabody, MA.

References

[1] A.K. Geim and I.V. Grigorieva, Nature **499**, 419 (2013).
[2] C.R. Dean, A.F. Young, I. Meric, C. Lee, L. Wang, S. Sorgenfrei, K. Watanabe, T. Taniguchi, P. Kim, K.L. Shepard, and J. Hone, Nat. Nanotechnol. **5**, 722 (2010).
[3] A.V. Kretinin, Y. Cao, J.S. Tu, G.L. Yu, R. Jalil, K.S. Novoselov, S.J. Haigh, A. Gholinia, A. Mishchenko, M. Lozada, T. Georgiou, C.R. Woods, F. Withers, P. Blake, G. Eda, A. Wirsig, C. Hucho, K. Watanabe, T. Taniguchi, A.K. Geim, and R.V. Gorbachev, Nano Lett. **14**, 3270 (2014).
[4] S.J. Haigh, A. Gholinia, R. Jalil, S. Romani, L. Britnell, D.C. Elias, K.S. Novoselov, L.A. Ponomarenko, A.K. Geim, and R. Gorbachev, Nat. Mater. **11**, 764 (2012).
[5] R. Decker, Y. Wang, V.W. Brar, W. Regan, H.-Z. Tsai, Q. Wu, W. Gannett, A. Zettl, and M.F. Crommie, Nano Lett. **11**, 2291 (2011).
[6] A. Reina, H. Son, L. Jiao, B. Fan, M.S. Dresselhaus, Z. Liu, and J. Kong, J. Phys. Chem. C **112**, 17741 (2008).
[7] J. Xue, J. Sanchez-Yamagishi, D. Bulmash, P. Jacquod, A. Deshpande, K. Watanabe, T. Taniguchi, P. Jarillo-Herrero, and B.J. LeRoy, Nat. Mater. **10**, 282 (2011).
[8] L. Britnell, R.V. Gorbachev, R. Jalil, B.D. Belle, F. Schedin, A. Mishchenko, T. Georgiou, M.I. Katsnelson, L. Eaves, S.V. Morozov, N.M.R. Peres, J. Leist, A.K. Geim, K.S. Novoselov, and L.A. Ponomarenko, Science **335**, 947 (2012).
[9] L. Britnell, R.M. Ribeiro, A. Eckmann, R. Jalil, B.D. Belle, A. Mishchenko, Y.-J. Kim, R.V. Gorbachev, T. Georgiou, S.V. Morozov, A.N. Grigorenko, A.K. Geim, C. Casiraghi, A.H.C. Neto, and K.S. Novoselov, Science **340**, 1311 (2013).
[10] A.S. Mayorov, R.V. Gorbachev, S.V. Morozov, L. Britnell, R. Jalil, L.A. Ponomarenko, P. Blake, K.S. Novoselov, K. Watanabe, T. Taniguchi, and A.K. Geim, Nano Lett. **11**, 2396 (2011).
[11] L.A. Ponomarenko, A.K. Geim, A.A. Zhukov, R. Jalil, S.V. Morozov, K.S. Novoselov, I.V. Grigorieva, E.H. Hill, V.V. Cheianov, V.I. Fal'ko, K. Watanabe, T. Taniguchi, and R.V. Gorbachev, Nat. Phys. **7**, 958 (2011).
[12] L. Wang, I. Meric, P.Y. Huang, Q. Gao, Y. Gao, H. Tran, T. Taniguchi, K. Watanabe, L.M. Campos, D.A. Muller, J. Guo, P. Kim, J. Hone, K.L. Shepard, and C.R. Dean, Science **342**, 614 (2013).
[13] R.V. Gorbachev, J.C.W. Song, G.L. Yu, A.V. Kretinin, F. Withers, Y. Cao, A. Mishchenko, I.V. Grigorieva, K.S. Novoselov, L.S. Levitov, and A.K. Geim, Science **346**, 448 (2014).
[14] H.J. Leamy, J. Appl. Phys. **53**, R51 (1982).
[15] T.G. Sparrow and U. Valdrèg, Philos. Mag. **36**, 1517 (1977).
[16] K.L. Bunker, Ph.D. thesis, North Carolina State University, 2005.
[17] W.J. Yu, Y. Liu, H. Zhou, A. Yin, Z. Li, Y. Huang, and X. Duan, Nat. Nanotechnol. **8**, 952 (2013).
[18] P. Blake, E.W. Hill, A.H.C. Neto, K.S. Novoselov, D. Jiang, R. Yang, T.J. Booth, and A.K. Geim, Appl. Phys. Lett. **91**, 063124 (2007).
[19] S.W. Smith, *The Scientist and Engineer's Guide to Digital Signal Processing* (California Tech. Pub, San Diego, CA, 1997).
[20] See supplemental material at [URL will be inserted by AIP] for resolution estimates on linear intensity greyscale versions of Figures 2 and 3.